Metals and Materials International (2019) 25:372–380
https://doi.org/10.1007/s12540-018-0204-6

High-Strength AZ91 Alloy Fabricated by Rapidly Solidified Flaky Powder Metallurgy and Hot Extrusion

Taekyung Lee[1] · Michiaki Yamasaki[2] · Yoshihito Kawamura[2] · Jongbin Go[3] · Sung Hyuk Park[3]

Received: 24 August 2018 / Accepted: 16 October 2018 / Published online: 12 November 2018

Abstract
A high-strength AZ91 alloy is produced via hot extrusion using flakes fabricated through the rapidly solidified flaky powder metallurgy. The AZ91 alloy flakes have an extremely fine dendritic structure without any second-phase particles owing to the fast cooling rate during solidification; these microstructural features considerably promote dynamic recrystallization and precipitation behaviors during extrusion process. As a result, the AZ91 alloy extruded using the flakes exhibits an almost fully recrystallized microstructure with a very small average grain size of 1.2 μm owing to an increase in the number of nucleation sites for recrystallization, and it shows a high microstructural homogeneity owing to the numerous $Mg_{17}Al_{12}$ precipitates uniformly distributed throughout the material. This extruded AZ91 alloy has a tensile yield strength of 345 MPa, ultimate tensile strength of 417 MPa, and total elongation of 5.6%. These superior tensile strengths are mainly attributed to the combined effects of precipitation hardening caused by abundant fine precipitates and grain boundary hardening caused by fine recrystallized grains.

Keywords AZ91 · Flake · Rapid solidification · Extrusion · Recrystallization

1 Introduction

Mg alloys have been considered as a promising material in the transportation industry owing to their low weight, which is an advantage from the perspectives of improving the energy efficiency of vehicles and reducing their carbon dioxide emissions. In particular, extruded Mg alloys have recently attracted considerable attention because they have superior mechanical properties as compared to their cast Mg counterparts, and controlling the process parameters of extrusion is easier than that of rolling. However, the strengths of extruded Mg alloys are still lower than those of high-strength Al alloys such as the 2xxx, 7xxx, and 8xxx series alloys; this eventually reduces the weight-saving benefits offered by Mg alloys and limits their application range. Hence, many studies have been conducted to develop high-strength extruded Mg alloys. Recently, it was reported that extruded Mg alloys containing more than 10 wt% of a combination of Gd and Y possess ultrahigh tensile yield strength (TYS)—higher than 450 MPa [1, 2]. However, the addition of such a large amount of expensive rare-earth (RE) elements significantly increases the cost of the final products, thereby lowering their cost competitiveness and posing challenges to their application as components of mass-produced vehicles.

Rapid solidification is an effective method for reducing grain size and solute segregation in Mg alloys and for increasing their solid solubility and chemical homogeneity [3, 4]. The powder metallurgy approach is widely used in the rapid solidification process; however, it often poses a high risk of explosion owing to the highly flammable nature of Mg powders [5]. To mitigate this risk and ensure safety, using additional process equipment is necessary, which increases the complexity of the manufacturing process and reduces productivity. An alternative technique to overcome these problems is rapidly solidified flaky powder metallurgy (RS FP/M), also called rapidly solidified ribbon

✉ Michiaki Yamasaki
yamasaki@gpo.kumamoto-u.ac.jp

✉ Sung Hyuk Park
sh.park@knu.ac.kr

[1] School of Mechanical Engineering, Pusan National University, Busan 46241, Republic of Korea

[2] Magnesium Research Center, Kumamoto University, Kumamoto 860-8555, Japan

[3] School of Materials Science and Engineering, Kyungpook National University, Daegu 41566, Republic of Korea

consolidation [6, 7]. This method produces RS metal flakes instead of powders, which can be sealed into a Cu capsule and then extruded. The RS FP/M technique facilitates the manufacturing of extruded bulk rods at an industrial scale while maintaining a fine-grained structure under safer conditions than those in conventional powder metallurgy.

Most previous studies applied the RS FP/M technique to Mg–Zn–RE alloys and their variants containing a long-period stacking ordered (LPSO) structure [3, 6–8]. The reported alloys exhibited remarkable improvements in strength at room temperature and high temperatures, as well as high superplasticity and corrosion resistance. The present study aims to demonstrate the capability of this advanced technique for non-LPSO Mg alloys. Recently, we successfully conferred a high strain-rate superplasticity to a commercially available Mg alloy through this technique [9]. Nevertheless, fundamental characteristics at room temperature have yet to be clarified. To this end, the RS FP/M technique is applied to an AZ91 alloy, which is a commercially used, highly alloyed, Mg–Al-based alloy. The microstructure of AZ91 flakes fabricated via the RS FP/M technique is analyzed through a comparison with that of an AZ91 billet fabricated via conventional ingot metallurgy. The tensile properties of the AZ91 alloy rod fabricated via extrusion using the flakes are investigated, and the strengthening mechanisms responsible for the high strength of the extruded alloy are discussed on the basis of its microstructural characteristics.

2 Experimental Procedure

High-purity ingots with the chemical composition Mg–9Al–1Zn (wt%) were melted in Ar atmosphere in a high-frequency electrical furnace. RS ribbons were produced by a single-roller melt-spinning method in an argon atmosphere with ~ 1 mm width, 20–30 μm thickness, and a few meters length. The roll circumferential velocity and cooling rate were 42 m s^{-1} and 1.4×10^5 °C s^{-1}, respectively. These ribbons were then cut into RS flakes with 10–20 mm length. A large-sized RS AZ91 bulk alloy was manufactured by consolidation of RS flakes. The flakes were packed into a cylindrical Cu can of length 60 mm, external diameter 31 mm, and wall thickness 1 mm. They were then compacted under a compressive load of 20 MPa, followed by degassing at 250 °C for 15 min. The green density after the compaction was estimated as 1.78 g cm^{-2}. Prior to extrusion, the degassed can and the extrusion die were heated to the extrusion temperature of 350 °C for 20 min. Extrusion was conducted at 350 °C with a ram speed of 2.5 mm s^{-1} and an extrusion ratio of 10. The Cu surface was completely eliminated before microstructural and tensile analyses. An AZ91 billet was fabricated via conventional ingot metallurgy for comparing its microstructure with that of the RS-AZ91 flakes. This material was cast into a cylindrical permanent mold with a diameter of 80 mm and length of 300 mm.

The microstructures of the RS flakes and the extruded alloy were characterized using optical microscopy (OM), scanning electron microscopy (SEM), and electron backscatter diffraction (EBSD) analysis. Microstructural samples were cut with a low-speed saw to minimize the generation of residual stress. The samples were mechanically polished using 800–4000-grit abrasive papers and then processed further depending on the test. SEM samples were chemically etched in a solution containing 70 ml of picric acid, 10 ml of acetic acid, and 10 ml of distilled water. EBSD samples were additionally polished through ion milling at 6 kV for 8 h. The TexSEM Laboratories orientation imaging microscopy (TSL OIM) analysis 5 software was used to analyze the EBSD data, and only those data points that possessed a high confidence index (> 0.1) were used to ensure the reliability of the analysis results.

The tensile properties of the extruded alloy were evaluated at an initial strain rate of 5×10^{-4} s^{-1} using a round specimen with a gage diameter of 2.5 mm and gage length of 12.4 mm. The tensile axis was parallel to the extrusion direction (ED). The tensile tests were repeated thrice for each material to obtain reliable data. The TYS, ultimate tensile strength (UTS), and total elongation (EL) were presented as average values with standard deviation; the TYS was determined as the value at 0.2% of the offset stress. The tensile strain was measured precisely using an optical extensometer connected to the tensile testing machine.

3 Results and Discussion

Optical and SEM micrographs of the RS-AZ91 flake fabricated using the RS FP/M technique are shown in Fig. 1a and b, respectively; for comparison, those of the cast AZ91 billet fabricated using the conventional mold-casting process are shown in Fig. 1c, d, respectively. The micrographs show that the RS flake and the cast billet have two distinct differences. First, even though both materials exhibit a dendritic structure—that is commonly observed in cast metals—their sizes are considerably different. The cast billet shows a coarse structure with an average grain size of 376 μm, whereas the RS flake has an extremely fine structure without any distinguishable grain boundaries. The secondary dendrite arm spacing (SDAS) of the RS flake (0.12 μm) is only ~ 1/220 times that of the cast billet (26 μm), which means that the RS FP/M technique greatly refines the dendritic structure of the AZ91 alloy. The SDAS of cast metal materials is known to be proportional to the rate of heat removal from the mold during solidification; therefore, higher cooling rates lead to a smaller dendritic structure [10, 11]. In addition, as the

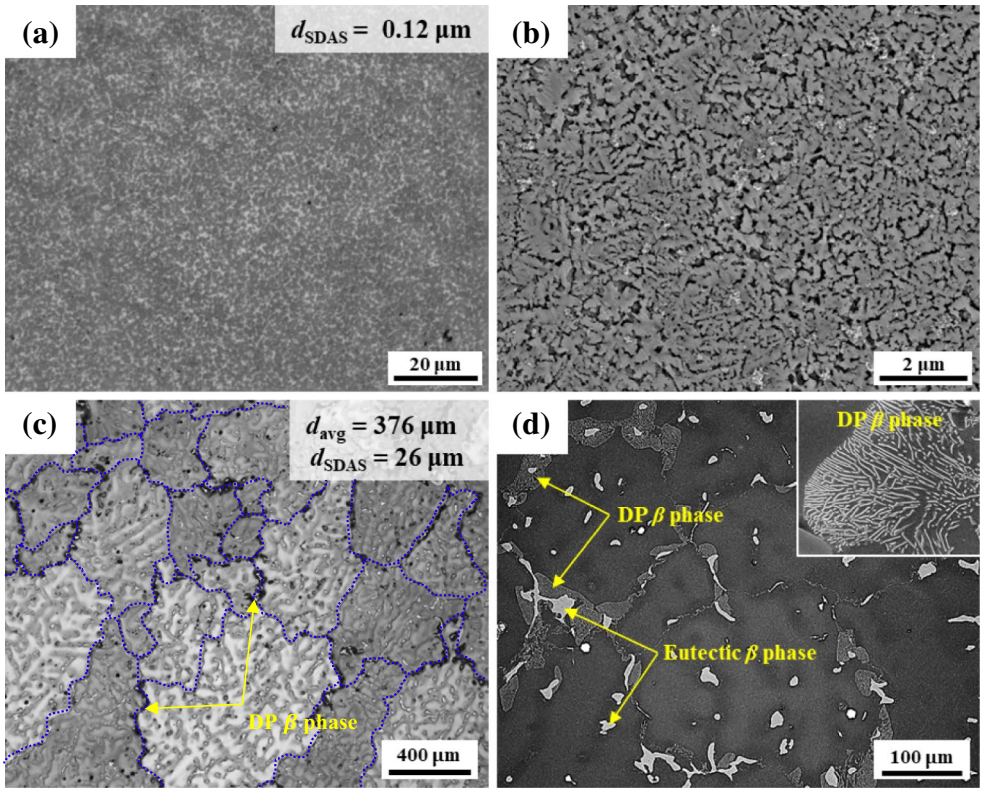

Fig. 1 **a**, **c** OM and **b**, **d** SEM micrographs of **a**, **b** AZ91 flake produced via RS FP/M technique and **c**, **d** AZ91 billet fabricated via conventional mold casting. The inset in (**d**) is an enlarged image showing the lamellar structure of discontinuous precipitates (DP). d_{avg} and d_{SDAS} denote the average grain size and average secondary dendrite arm spacing, respectively. Blue dotted lines in (**c**) indicate the grain boundaries

cooling rate during the casting process decreases, the time required for the disappearance of small dendrite arms—which occurs to reduce the total surface energy of the material—increases; this consequently leads to an increase in the SDAS [12, 13]. In other words, the first major microstructural difference between the RS flake and the cast billet is the drastic refinement of the dendritic structure in the RS flake.

The second major difference is the presence or absence of the β-$Mg_{17}Al_{12}$ phase. In the cast billet, large particles of the eutectic $Mg_{17}Al_{12}$ phase are distributed along the grain boundaries and in regions between the dendrite arms (represented as the bright phase in Fig. 1d). Moreover, $Mg_{17}Al_{12}$ phase precipitates with a fine lamellar structure are also present along the grain boundaries (represented as the gray phase in Fig. 1d). Unlike the eutectic $Mg_{17}Al_{12}$ phase particles formed during solidification, these fine-lamellar structured precipitates—which have a morphology similar to the typical lamellar pearlite structure in steel—are formed via discontinuous precipitation during the cooling after solidification [14, 15]. Owing to the presence of this considerable amount of $Mg_{17}Al_{12}$ phase particles and precipitates, homogenization heat treatment must be performed before the extrusion process to dissolve the second phase into the α-Mg matrix. In contrast, the RS flake does not contain the $Mg_{17}Al_{12}$ phase (Fig. 1b) because insufficient time is available for the formation of the second phase during solidification of the molten metal owing to the extremely fast cooling rate. Accordingly, all Al atoms in the RS flake exist in the dissolved state within the α-Mg matrix without forming any second-phase particles. Moreover, this increase in the dissolved Al content decreases the lattice parameters of the hexagonal crystal structure, which in turn contributes to reduction in the SDAS of the RS flake [5]. This supersaturation of the alloying elements and suppression of the formation of intermetallic compounds are advantages of the RS FP/M technique [4, 5, 16]. In addition, as shown in the EDS maps of the RS flakes in Fig. 2, the solute atoms of Al and Zn, which are alloying elements added to this alloy, are uniformly distributed without micro-segregation; this indicates that the RS flakes have a high compositional homogeneity. Therefore, extrusion using RS flakes can be conducted without any prior homogenization treatment owing to their ultrafine and homogeneous microstructure, which is devoid of any second-phase particles and solute segregation.

The microstructural characteristics of the extruded RS-AZ91 alloy as obtained via EBSD analysis are shown

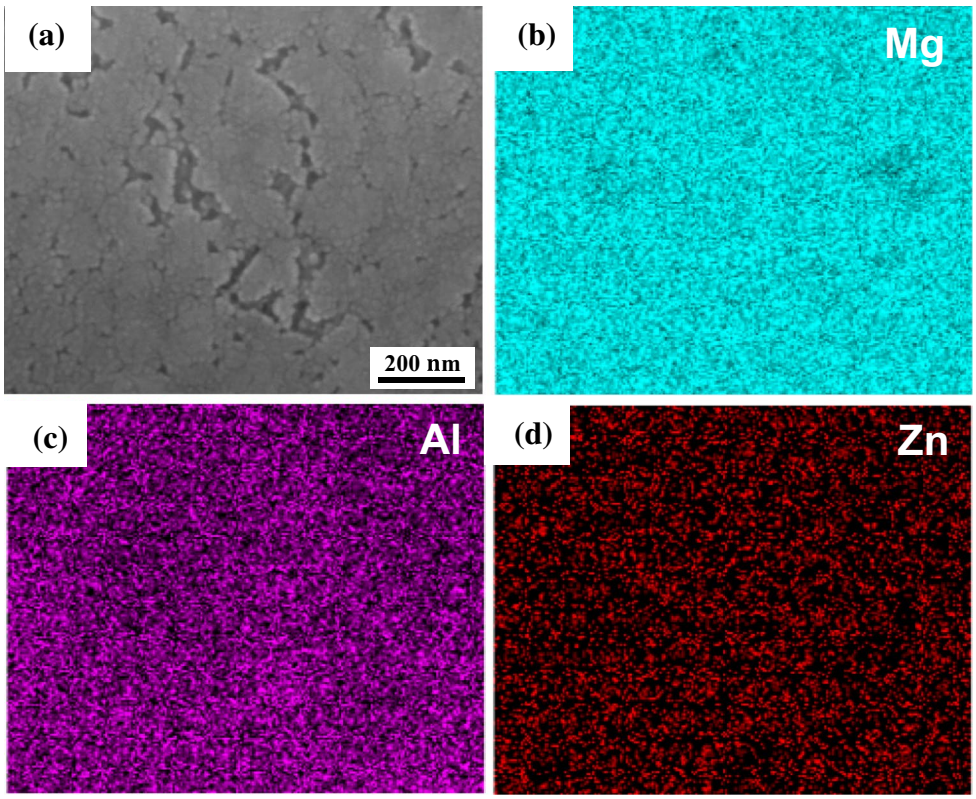

Fig. 2 **a** SEM image of AZ91 flake produced via RS FP/M technique and corresponding EDS maps of **b** Mg, **c** Al and **d** Zn

in Fig. 3. The alloy exhibits an almost fully dynamically recrystallized (DRXed) microstructure, in which the area fraction of the DRXed grains is 96.8% (Fig. 3a–c). In Mg alloys, the area fraction of DRXed grains formed during hot deformation depends strongly on the applied strain [17, 18]; as the strain increases, the dynamic recrystallization (DRX) fraction increases owing to an increase in the internal strain energy, which is the driving force for recrystallization. Given that a large amount of deformation is generally applied in a single pass during extrusion, the strain applied during extrusion in this study was relatively small (~2.3) owing to the low extrusion ratio of 10. A previous study reported that an extruded AZ91 alloy exhibited a partially DRXed grain structure when an AZ91 billet fabricated using the mold casting process was extruded at a relatively large strain of ~3.2 at the same temperature as that employed in the present study (350 °C) [19]. In contrast, in the present study, almost complete recrystallization occurred during extrusion using the RS-AZ91 flakes, despite the smaller imposed strain. As the microstructure of the initial material becomes finer, the number of nucleation sites for recrystallization during hot extrusion increases, leading to an increase in the DRX fraction of the extruded material [20]. Accordingly, the enhanced DRX behavior observed in the extruded RS-AZ91 alloy in the present study is attributed to the significantly refined microstructure of the flakes.

The equiaxed DRXed grains of the extruded RS-AZ91 alloy are extremely fine—just 1.1 μm in size (Fig. 3c). Moreover, the elongated unDRXed grains are also just 5.9 μm in size (Fig. 3b). Consequently, the average grain size of the extruded alloy is 1.2 μm (Fig. 3d). This type of grain structure is consistent with that of other RS-AZ91 samples exhibiting a high-strain-rate superplasticity [9]. Because the growth of grains newly formed by DRX is caused by the diffusion of atoms at grain boundaries, the final size of the DRXed grains is closely related to the deformation temperature [21]. Our previous study showed that the average size of the DRXed grains in an AZ91 alloy extruded at 350 °C using a homogenized billet was 20.1 μm [19], which is ~18.3 times that of the extruded RS-AZ91 alloy (1.1 μm) and ~3.4 times the average size of the unDRXed grains in this extruded alloy (5.9 μm). In another study [20], when the homogenized AZ91 billet was extruded at a relatively low temperature of 250 °C, the DRXed grains in the extruded alloy were of a small size (1.3 μm), similar to those in the extruded RS-AZ91 alloy (1.1 μm). However, in the previous extruded alloy, a considerable amount of large unDRXed grains—whose area fraction and average size were 26.5% and 58.6 μm, respectively—remained owing to the suppression of DRX behavior by the low deformation temperature [20]. In contrast, the extruded RS-AZ91 alloy possesses a high DRX fraction and a fine grain size simultaneously. In addition, the DRXed grains exhibit a narrow size

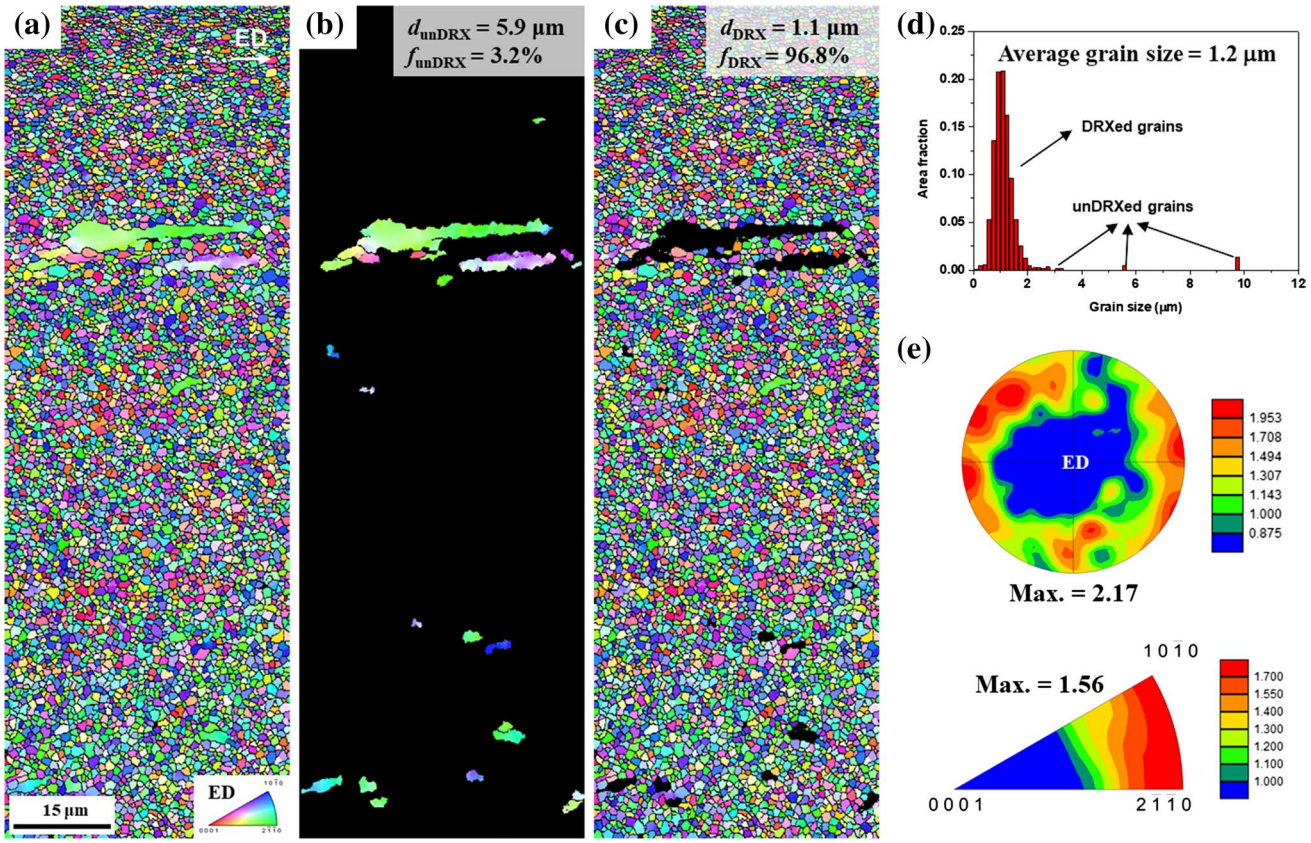

Fig. 3 Microstructure and texture of extruded RS-AZ91 alloy: inverse pole figure maps of **a** total, **b** unDRXed and **c** DRXed regions; **d** grain size distribution; and **e** (0002) pole figure and ED inverse pole figure. d_{DRX} and d_{unDRX} denote the average grain sizes of the DRXed and unDRXed regions, respectively. f_{DRX} and f_{unDRX} denote the area fractions of the DRXed and unDRXed regions, respectively

distribution range of ~ 0.5–2 μm (Fig. 3d), which indicates that the microstructure of the extruded RS-AZ91 alloy is uniform.

Such small grain size and high microstructural uniformity are attributed to the precipitates formed during extrusion. SEM micrographs of the extruded RS-AZ91 alloy are shown in Fig. 4a–c. These micrographs show that abundant fine precipitates, ~ 300–700 nm in size, are homogeneously distributed throughout the material. In the unDRXed region, smaller precipitates (~ 100–200 nm) are observed (Fig. 4b). The XRD results reveal that all these precipitates are the $Mg_{17}Al_{12}$ phase formed via dynamic precipitation during extrusion (Fig. 4d). Dynamically formed precipitate particles can effectively suppress the growth of DRXed grains through the grain boundary pinning phenomenon during hot extrusion. Indeed, the $Mg_{17}Al_{12}$ precipitates are located

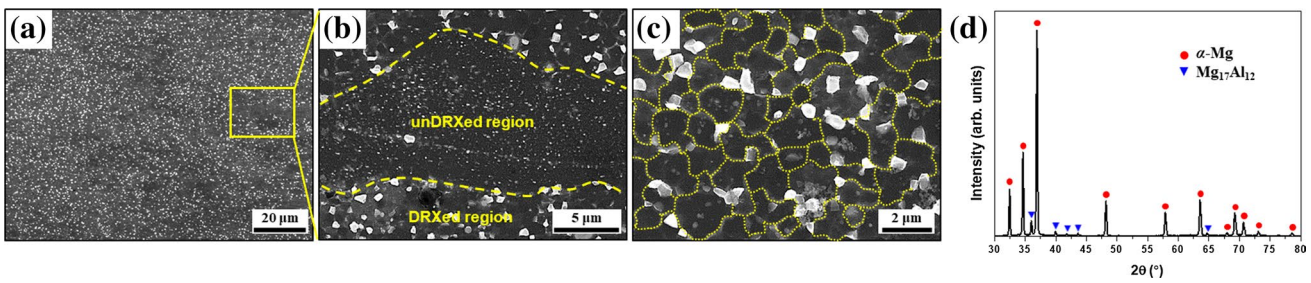

Fig. 4 SEM micrographs of extruded RS-AZ91 alloy showing **a** overall distribution of precipitates, **b** fine precipitates in unDRXed region, and **c** grain boundary pinning of precipitates in DRXed region. **d** XRD pattern of extruded RS-AZ91 alloy. Yellow dotted lines in **c** indicate the grain boundaries of DRXed grains. (Color figure online)

mostly at the boundaries of the DRXed grains (Fig. 4c). This inhibition of grain growth by the dynamic precipitates and the resultant grain refinement have been widely reported in various extruded Mg alloys such as Mg–Al, Mg–Sn, Mg–Zn, and Mg–RE alloy systems [22–27].

The most remarkable feature of the precipitates of the extruded RS-AZ91 alloy is their homogeneous distribution. In the abovementioned extruded AZ91 alloy, fabricated via extrusion using a conventional billet at 350 °C, the $Mg_{17}Al_{12}$ precipitates are formed locally in the form of precipitate bands (~40–100 μm in width) arranged parallel to the ED [19]. Numerous precipitates exist in the precipitate bands, whereas few precipitates exist in the regions between the precipitate bands. This inhomogeneous distribution of the precipitates causes a difference in the DRXed grain size between the precipitate-rich region (i.e., precipitate bands) and the precipitate-scarce region. That is, the grains become much larger in the precipitate-scarce region owing to weakening of the grain boundary pinning effect, which consequently leads to a nonuniform grain structure of the extruded alloy. By contrast, in the extruded RS-AZ91 alloy, homogenous precipitate formation without locally concentrated distributions improves the microstructural uniformity of the extruded material. Similar to the promoted DRX behavior of the RS-AZ91 alloy, this homogeneous formation of precipitates is also due to the fine microstructure and uniform chemical composition of the initial RS flakes. As shown in Fig. 1c, d, the interspacing between the $Mg_{17}Al_{12}$ phase particles of the cast AZ91 billet is considerably large (~50–100 μm) owing to the coarse grain size. Accordingly, although homogenization treatment is performed at temperatures lying in the α-Mg single-phase region on the equilibrium phase diagram, it takes a long time for the $Mg_{17}Al_{12}$ phase formed during solidification or subsequent cooling to fully dissolve into the α-Mg matrix; the dissolved Al solute atoms also take a long time to distribute uniformly in the matrix through bulk diffusion. Hence, in a homogenized AZ91 billet, a locally high concentration of Al solute atoms (i.e., solute segregation) is observed around the sites where the initial $Mg_{17}Al_{12}$ phase exists owing to insufficient diffusion of the Al atoms during heat treatment [28]. This inhomogeneous distribution of solute atoms in a homogenized billet eventually causes localized formation of the dynamic precipitates during extrusion (i.e., precipitate bands) [17]. In contrast, in the RS-AZ91 flakes, no $Mg_{17}Al_{12}$ phase particles are formed owing to the rapid cooling rate. In addition, even though a compositional difference may exist between the dendritic and the interdendritic regions, this difference does not cause inhomogeneous distribution of dynamic precipitates because the average width of the dendrites is only ~200 nm. Therefore, the Al solute atoms supersaturated in the RS flakes having an extremely fine structure are precipitated uniformly as $Mg_{17}Al_{12}$ particles throughout the material during extrusion, which, in turn, results in a fine and uniform grain structure of the extruded RS-AZ91 alloy owing to the effective inhibition of grain growth by the evenly distributed precipitates.

Figure 5 shows the tensile stress–strain curve and the corresponding values of the tensile properties of the extruded RS-AZ91 alloy. The alloy exhibits a TYS of 345 MPa, UTS of 417 MPa, and EL of 5.6%. Extruded AZ91 alloys fabricated using a conventional billet have TYSs of 130–262 MPa and UTSs of 308–364 MPa [19, 29–31]. Therefore, it is clear that the extruded RS-AZ91 alloy has significantly higher strengths, especially TYS, as compared with the conventionally extruded AZ91 alloys. Moreover, the strengths of the extruded RS-AZ91 alloy are higher than even those of the AZ91 alloys subjected to equal-channel angular pressing (ECAP), which is a representative severe plastic deformation process (TYSs of 164–290 MPa and UTSs of 293–417 MPa), while maintaining comparable ductility (ELs of 2–9%) [29, 30, 32].

The strength of extruded Mg alloys is known to be governed by the combined effects of several strengthening mechanisms: texture hardening, dispersion hardening, solid-solution hardening, strain hardening, precipitation hardening, and grain boundary hardening. From the perspective of texture hardening, the extruded RS-AZ91 alloy exhibits a basal fiber texture in which the basal planes of most grains are oriented parallel to the ED (Fig. 3e). This texture is typical of extruded Mg alloys that do not contain RE alloying elements. Because the maximum texture intensity of the extruded RS-AZ91 alloy is relatively low (2.17 and 1.56 in the (0001) pole figure and ED inverse pole figure, respectively), the substantially higher strength of the RS-AZ91 alloy relative to that of the conventional AZ91 alloys is not due to the texture hardening effect. In addition, dispersion

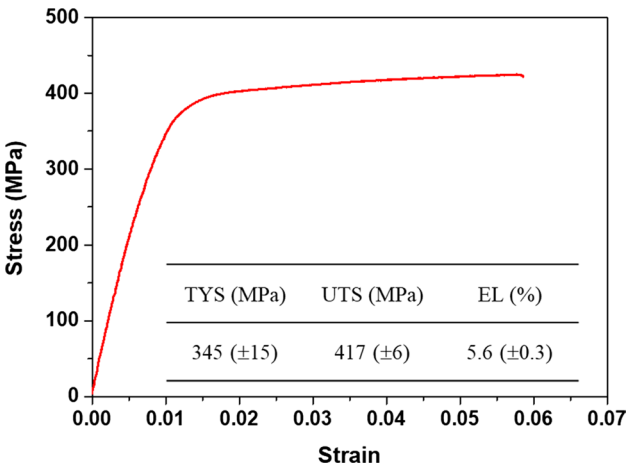

Fig. 5 Tensile stress–strain curve of extruded RS-AZ91 alloy. TYS, UTS, and EL denote the tensile yield strength, ultimate tensile strength, and total elongation, respectively

hardening caused by undissolved second-phase particles is also precluded because the RS-AZ91 flakes do not have any second phase. The solubility limit of alloying elements in metallic materials varies with temperature; accordingly, the solid-solution hardening effect caused by the Al solute atoms dissolved in the α-Mg matrix is considered to be identical in the extruded RS-AZ91 alloy and conventional AZ91 alloys extruded under the same processing conditions.

The extruded RS-AZ91 alloy contains a small amount of the unDRXed grains, which are continuously deformed during extrusion and can contribute to tensile strengthening through a strong strain-hardening effect. Figure 6a, b show the results of the misorientation line profile in the largest unDRXed grain among those observed in the extruded RS-AZ91 alloy. The crystal orientation changes gradually with the position in the grain, and the point-to-origin orientation difference within one unDRXed grain is up to 27°. This indicates that the lattice of the unDRXed grains is severely distorted because the strain accumulated during extrusion cannot dissipate through the DRX mechanism. This lattice distortion can also be confirmed by comparing the average values of the grain orientation spread (GOS) and kernel average misorientation (KAM)—both of which represent stored internal strain energy [33]—of the DRXed and unDRXed regions. The average GOS value of the unDRXed region is ~ 10 times that of the DRXed region (7.97 and 0.80 for the unDRXed and DRXed regions, respectively; see Fig. 6c), and the average KAM value of the unDRXed region is higher as well (1.31 and 0.87 for the unDRXed and DRXed regions, respectively; see Fig. 6d). Therefore, although the grain boundary hardening effect is somewhat weaker in the relatively coarse unDRXed grains than that in the fine DRXed grains, the strain hardening effect is stronger in the unDRXed grains owing to their high internal strain energy. However, this strain hardening effect does not play a decisive role in enhancing the strength of the extruded alloy because the area fraction of the unDRXed grains is small.

The uniformly distributed fine $Mg_{17}Al_{12}$ precipitates can significantly contribute toward improving the strength of the extruded RS-AZ91 alloy. According to the Orowan equation, the Orowan stress induced by second-phase particles increases with decreasing interparticle spacing [21].

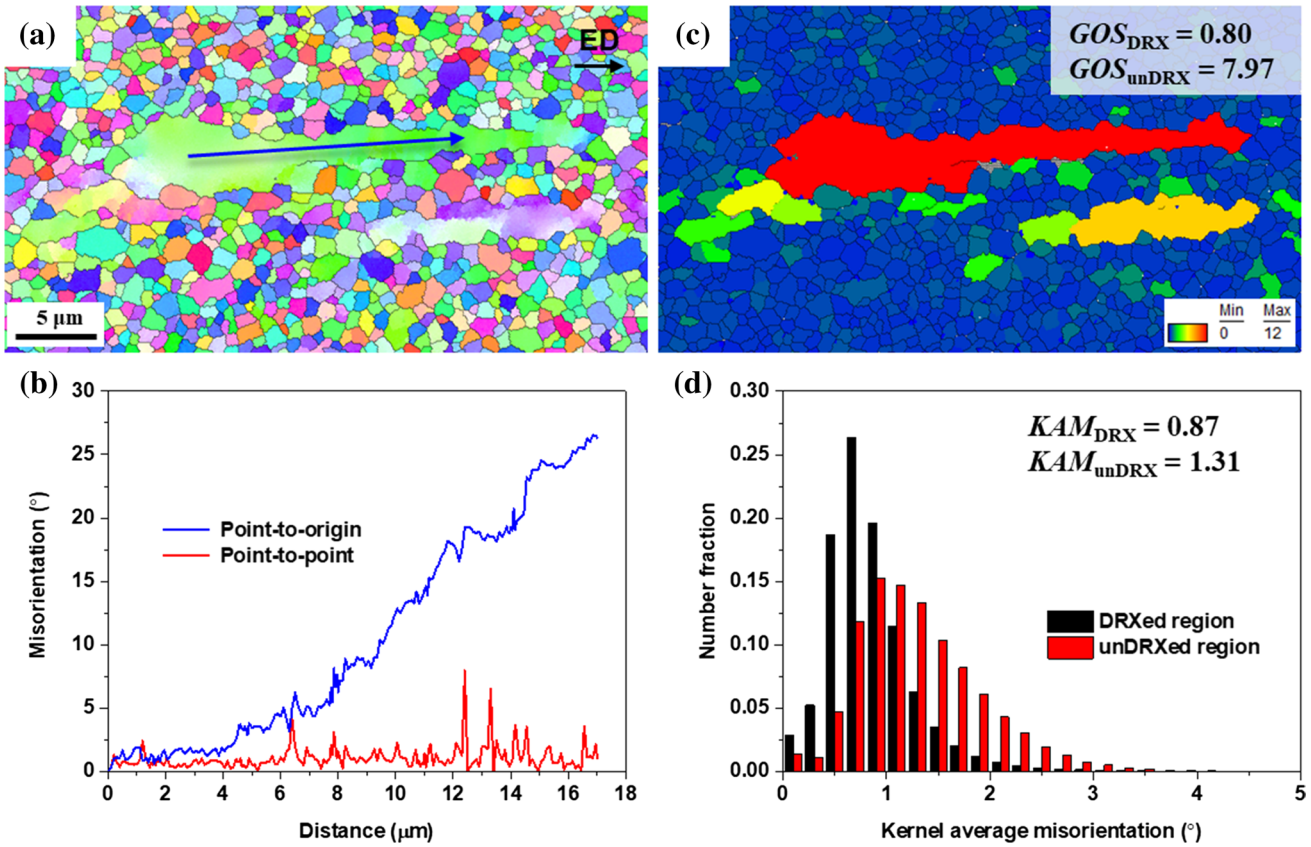

Fig. 6 Microstructural analysis of unDRXed grain: **a** inverse pole figure map, **b** misorientation line profiles along direction indicated by blue arrow in **a**, **c** grain orientation spread (GOS) map of region containing unDRXed grains and **d** distribution of kernel average misorientation (KAM) values of DRXed and unDRXed regions. GOS_{DRX} and GOS_{unDRX} denote the average GOS values of the DRXed and unDRXed regions, respectively. KAM_{DRX} and KAM_{unDRX} denote the average KAM values of the DRXed and unDRXed regions, respectively

In conventionally extruded AZ91 alloys, $Mg_{17}Al_{12}$ precipitates are distributed locally in precipitate bands. The average interparticle spacing in the precipitate bands of the conventional AZ91 alloy extruded at the same temperature as that employed in the present study (350 °C) using a homogenized billet is nearly identical to that of the extruded RS-AZ91 alloy (~ 500 nm) [19]. However, the area fraction of the precipitate bands, which cause a meaningful precipitation hardening effect, of the conventional AZ91 alloy is only 8.4%; therefore, the hardening effect by the $Mg_{17}Al_{12}$ precipitates is very limited in this alloy because the precipitate-scarce region occupies most of the extruded material. In contrast, in the extruded RS-AZ91 alloy, finer and more abundant precipitates are formed over the entire material, not in the localized region. This is attributed to the increased number of nucleation sites for dynamic precipitation resulting from the ultrafine microstructure and homogeneous solute distribution of the flakes. Accordingly, a considerable precipitation hardening effect occurs in the extruded RS-AZ91 alloy, which plays an important role in improving its strength.

In addition to the abundant $Mg_{17}Al_{12}$ precipitates, the fine DRXed grain structure of the extruded RS-AZ91 alloy—which is induced by enhancement of the DRX and grain boundary pinning behaviors—also leads to considerable grain boundary hardening during tensile deformation. As the value of the Hall–Petch hardening coefficient of extruded Mg–Al–Zn alloys (e.g., AZ31, AZ61, and AZ80) at room temperature increases with increasing Al content [34], a remarkable increase in the Hall–Petch stress is caused by grain refinement in the AZ91 alloy, which has a high Al content of 9 wt%. Although a few unDRXed grains exist in the extruded RS-AZ91 alloy, their amount and size are small (their area fraction and average size are 3.2% and 5.9 μm, respectively; see Fig. 3b). Therefore, they do not cause meaningful weakening of the grain boundary hardening effect caused by the refined microstructure of the material.

The average grain size and TYS of the abovementioned conventional AZ91 alloy extruded at 350 °C using a homogenized billet are 20.1 μm and 211 MPa [19], whereas those of the extruded RS-AZ91 alloy are 1.2 μm and 345 MPa, respectively. According to the Hall–Petch equation, the increase in the Hall–Petch hardening stress ($\Delta\sigma_{H-P}$) caused by the refined grain structure of the RS-AZ91 alloy relative to the conventional AZ91 alloy can be calculated as $\Delta\sigma_{H-P} = k(d_{RS\text{-}AZ91}^{-0.5} - d_{Ext\text{-}AZ91}^{-0.5})$, where k is the Hall–Petch coefficient, and $d_{RS\text{-}AZ91}$ and $d_{Extr\text{-}AZ91}$ are the average grain sizes of the RS-AZ91 alloy and conventional AZ91 alloy, respectively. Using a k value of 0.23 MPa $m^{1/2}$ for tension of the extruded AZ91 alloy [35] and the measured average grain sizes of the two extruded alloys, a strength improvement as high as 159 MPa can be achieved by grain refinement in the RS-AZ91 alloy compared with the conventional AZ91 alloy (i.e., $\Delta\sigma_{H-P}$). This calculated value is larger than the difference in the TYSs of both the alloys (134 MPa), which is probably because the lower texture hardening effect of the RS-AZ91 alloy than that of the conventional AZ91 alloy is reflected in the Hall–Petch hardening results (the maximum texture intensities in the ED inverse pole figure are 1.56 and 3.3 for the RS-AZ91 and conventional AZ91 alloys, respectively [19]). Even though the degree of the hardening effect due to grain refinement calculated by the Hall–Petch relation may not be accurate, it is certain that the fine grain structure with an average grain size of 1.2 μm of the RS-AZ91 alloy considerably contributes to its improved strength. Therefore, the high strength of the extruded RS-AZ91 alloy is mainly attributed to the outstanding effects of precipitation hardening due to the uniformly distributed fine $Mg_{17}Al_{12}$ precipitates and grain boundary hardening caused by the almost fully DRXed microstructure with extremely fine grains.

4 Conclusions

In this study, we demonstrated that the RS FP/M technique can produce second-phase-free AZ91 flakes with an ultrafine dendritic structure and that an AZ91 alloy fabricated by extruding these RS flakes exhibits a fine and homogeneous microstructure and superior tensile properties. Hot extrusion using the flakes leads to the promotion of DRX and dynamic precipitation behaviors during extrusion, which increases the area fraction of DRXed grains owing to the presence of an increased number of nucleation sites for DRX and decreases the DRXed grain size owing to enhanced grain boundary pinning by precipitates. Consequently, the extruded RS-AZ91 alloy has a larger DRX fraction, smaller grain size, more abundant precipitates, and higher microstructural homogeneity than AZ91 alloys fabricated conventionally by extruding cast billets. The considerably high strength of the extruded RS-AZ91 alloy is mainly attributed to the precipitation hardening and grain boundary hardening effects, which are caused by the abundance of fine $Mg_{17}Al_{12}$ precipitates distributed uniformly throughout the material and the significantly refined DRXed grains that occupy almost the entire area of the material, respectively.

Acknowledgements This work was supported by the National Research Foundation of Korea (NRF) grants funded by the Korean government (MSIP, South Korea) (Nos. 2016R1C1B2012140 and 2018R1C1B6002068).

References

1. T. Homma, N. Kunito, S. Kamado, Scr. Mater. **61**, 644–647 (2009)
2. W.W. Jian, G.M. Cheng, W.Z. Xu, H. Yuan, M.H. Tsai, Q.D. Wang, C.C. Koch, Y.T. Zhu, S.N. Mathaudhu, Mater. Res. Lett. **1**, 61–66 (2013)

3. Y. Kawamura, K. Hayashi, A. Inoue, T. Masumoto, Mater. Trans. **42**, 1172–1176 (2001)
4. E. Ayman, U. Junko, K. Katsuyoshi, Acta Mater. **59**, 273–282 (2011)
5. K.S. Govind, M.C. Nair, K. Mittal, R.K. Lal, C.S. Mahanti, Sivaramakrishnan. Mater. Sci. Eng. A **304–306**, 520–523 (2001)
6. M. Yamasaki, N. Hayashi, S. Izumi, Y. Kawamura, Corros. Sci. **49**, 255–262 (2007)
7. H. Okouchi, Y. Seki, T. Sekigawa, H. Hira, Y. Kawamura, Mater. Sci. Forum **638–642**, 1476–1481 (2010)
8. G. Garcés, G. Requena, D. Tolnai, P. Pérez, J. Medina, A. Stark, N. Schell, P. Adeva, Mater. Charact. **118**, 514–518 (2016)
9. T. Lee, M. Yamasaki, Y. Kawamura, Y. Lee, C.S. Lee, Mater. Lett. **234**, 245–248 (2019)
10. M.Ş. Turhal, T. Savaşkan, J. Mater. Sci. **38**, 2639–2646 (2003)
11. F.C. Campbell, *Phase Diagrams: Understanding the Basics* (ASM International, Materials Park, 2012)
12. J. Campbell, *Castings*, 2nd edn. (Butterworth-Heinemann, Oxford, 2003)
13. T.Z. Kattamis, J.C. Coughlin, M.C. Flemings, Trans. Met. Soc. AIME **239**, 1504–1511 (1967)
14. M.C. Zhao, M. Liu, G. Song, A. Atrens, Corros. Sci. **50**, 1939–1953 (2008)
15. J.Y. Li, J.X. Xie, Adv. Mater. Res. **264–265**, 66–71 (2011)
16. J. Cai, G.C. Ma, Z. Liu, H.F. Zhang, A.M. Wang, Z.Q. Hu, Mater. Sci. Eng. A **456**, 364–367 (2007)
17. C. Bettles, M. Barnett, *Advances in Wrought Magnesium Alloys: Fundamentals of Processing, Properties and Applications*, 1st edn. (Woodhead Publishing, Philadelphia, 2012)
18. Y. Chen, Q. Wang, J. Peng, C. Zhai, W. Ding, J. Mater. Process. Technol. **182**, 281–285 (2007)
19. S.H. Kim, J.U. Lee, Y.J. Kim, B.G. Moon, B.S. You, H.S. Kim, S.H. Park, Mater. Sci. Eng. A **703**, 1–8 (2017)
20. S.H. Park, J.H. Bae, S.H. Kim, J. Yoon, B.S. You, Metall. Mater. Trans. A **46**, 5482–5488 (2015)
21. G.E. Dieter, *Mechanical Metallurgy, SI Metrix edition* (McGraw-Hill, London, 1988)
22. S.W. Bae, S.H. Kim, J.U. Lee, W.K. Jo, W.H. Hong, W. Kim, S.H. Park, J. Alloys Compd. **766**, 748–758 (2018)
23. H.Y. Wang, J. Rong, G.J. Liu, M. Zha, C. Wang, D. Luo, Q.C. Jiang, Mater. Sci. Eng. A **698**, 249–255 (2017)
24. S.H. Kim, J.U. Lee, Y.J. Kim, J.G. Jung, S.H. Park, J. Alloys Compd. **751**, 1–11 (2018)
25. B. Wang, F. Pan, X. Chen, W. Guo, J. Mao, Mater. Sci. Eng. A **656**, 165–173 (2016)
26. Z. Yu, C. Xu, J. Meng, X. Zhang, S. Kamado, Mater. Sci. Eng. A **713**, 234–243 (2018)
27. S.H. Kim, J.G. Jung, B.S. You, S.H. Park, J. Alloys Compd. **695**, 344–350 (2017)
28. J.U. Lee, S.H. Kim, Y.J. Kim, S.H. Park, Mater. Sci. Eng. A **714**, 49–58 (2018)
29. K. Máthis, J. Gubicza, N.H. Nam, J. Alloys Compd. **394**, 194–199 (2005)
30. M. Mabuchi, Y. Chino, H. Iwasaki, T. Aizawa, K. Higashi, Mater. Trans. **42**, 1182–1189 (2001)
31. S.H. Kim, B.S. You, S.H. Park, J. Alloys Compd. **690**, 417–423 (2017)
32. B. Chen, D.L. Lin, L. Jin, X.Q. Zeng, C. Lu, Mater. Sci. Eng. A **483–484**, 113–116 (2008)
33. S.I. Wright, M.M. Nowell, D.P. Field, Microsc. Microanal. **17**, 316–329 (2011)
34. J. Bohlen, P. Dobroň, J. Swiostek, D. Letzig, F. Chmelík, P. Lukáč, K.U. Kainer, Mater. Sci. Eng. A **462**, 302–306 (2007)
35. C.H. Cáceres, C.J. Davidson, J.R. Griffiths, C.L. Newton, Mater. Sci. Eng. A **325**, 344–355 (2002)